CHEMISTRY
A EUROPEAN JOURNAL

DOI: 10.1002/chem.200903137

Facile and Controllable Synthesis of Monodisperse CaF_2 and CaF_2:Ce^{3+}/Tb^{3+} Hollow Spheres as Efficient Luminescent Materials and Smart Drug Carriers

Cuimiao Zhang, Chunxia Li, Chong Peng, Ruitao Chai, Shanshan Huang, Dongmei Yang, Ziyong Cheng, and Jun Lin*[a]

Abstract: Highly uniform and well-dispersed CaF_2 hollow spheres with tunable particle size (300–930 nm) have been synthesized by a facile hydrothermal process. Their shells are composed of numerous nanocrystals (about 40 nm in diameter). The morphology and size of the CaF_2 products are strongly dependent on experimental parameters such as reaction time, pH value, and organic additives. The size of the CaF_2 hollow spheres can be controlled from 300 to 930 nm by adjusting the pH value. Nitrogen adsorption–desorption measurements suggest that mesopores (av 24.6 nm) exist in these hollow spheres. In addition, Ce^{3+}/Tb^{3+}-codoped CaF_2 hollow spheres can be prepared similarly, and show efficient energy transfer from Ce^{3+} to Tb^{3+} and strong green photoluminescence of Tb^{3+} (541 nm, $^5D_4 \rightarrow {}^7F_5$ transition of Tb^{3+}, the highest quantum efficiency reaches 77%). The monodisperse CaF_2:Ce^{3+}/Tb^{3+} hollow spheres also have desirable properties as drug carriers. Ibuprofen-loaded CaF_2:Ce^{3+}/Tb^{3+} samples still show green luminescence of Tb^{3+} under UV irradiation, and the emission intensity of Tb^{3+} in the drug-carrier system varies with the released amount of ibuprofen, so that drug release can be easily tracked and monitored by means of the change in luminescence intensity. The formation mechanism and luminescent and drug-release properties were studied in detail.

Keywords: drug delivery · fluorides · hydrothermal synthesis · luminescence · nanostructures

Introduction

Hollow micro- and nanostructures have attracted considerable attention because of their unique properties (e.g., porous shell, low density, high surface-to-volume ratio, low coefficients of thermal expansion, and low refractive index) and widespread applications in drug-delivery carriers, efficient catalysis, sensors, active-material encapsulation, photonic crystals, and so on.[1–8] Various fabrication procedures for hollow structures have been developed. The general strategy for the synthesis of hollow spheres is a template-assisted process in which coating of templates with nanocrystals is followed by removal of the template, which can be hard (e.g., silica,[9,10] polymer latex spheres,[11,12] carbon spheres,[13,14] and metal nanoparticles)[15,16] or soft (e.g., emulsion droplets and/or micelles,[17–20] liquid drops,[21] vesicles,[22] and even gas bubbles[23]). In some case, the yields of hollow products obtained by template-assisted approaches are low, or the shells are not intact, which might lead to poor mechanical performance. Moreover, these methods tend to be rather complicated, with the obvious drawback that the removal process often compromises the structural integrity of the final products and limits the practical applications.[24] Therefore, it is still highly desirable to develop a facile one-step, mild, and cheap synthetic approaches to uniform inorganic hollow structures with defined shape, size, and composition.

Solid fluoride materials have attracted much attention due to their uncommon properties, such as low-energy phonons, high ionicity, electron-acceptor behavior, high resistivity, and anionic conductivity.[25–27] These properties lead to a wide range of potential optical applications in optics, biological labels, and lenses,[28,29] as well as components of insula-

[a] C. Zhang, C. Li, C. Peng, R. Chai, S. Huang, D. Yang, Z. Cheng, J. Lin
State Key Laboratory of Rare Earth Resource Utilization
Changchun Institute of Applied Chemistry
Chinese Academy of Sciences
Changchun 130022 (China)
and
Graduate University of the Chinese Academy of Sciences
Beijing 100049 (China)
Fax: (+86) 431-8569-8041
E-mail: jlin@ciac.jl.cn

Supporting information for this article is available on the WWW under http://dx.doi.org/10.1002/chem.200903137.

tors, gate dielectrics, wide-gap insulating overlayers, and buffer layers in semiconductor-on-insulator structures.[30] Among the various fluorides, calcium fluoride (CaF_2) has a low refractive index and a wide band gap ($E_g = 12.1$ eV) and is optically transparent over a wide wavelength range from mid-infrared to vacuum ultraviolet.[31,32] Therefore, CaF_2 is widely used in UV lithography, UV-transparent optical lenses, surface conditioning of glass, promoting agents for bone/tooth reconstruction, and biocompatible luminescent markers.[29,32,33] Moreover, CaF_2 is an attractive host for phosphors activated with rare earth ions (RE^{3+}), which display unique up/down-conversion luminescence properties arising from their 4f electron configuration.[26,33] Furthermore, RE^{3+} ions incorporated in the CaF_2 host lattice increase the refractive index with respect to pure CaF_2, which makes it very attractive as an active waveguide for optical integrated devices.[34] With a view to biological applications, Li et al reported that CaF_2 nanocubes can be functionalized by a simple chemical modification method for introduction rare earth ions into the host lattice, which endows CaF_2 with luminescent properties and provides new opportunities in diagnosis as a luminescent biological label.[33] However, this material has never been properly tested as a drug carrier. The conventional morphology and textural properties are expected to be the major limiting factors. Mesoporosity is necessary for drug carriers in many cases. Therefore, the design and development of luminescence-functionalized CaF_2 with uniform morphology and mesoporosity is of major interest.

Here we demonstrate a simple, template-free, and one-step strategy for the synthesis of hollow CaF_2 spheres with controllable size by a simple hydrothermal route. The external surface of the shell of the obtained CaF_2 hollow spheres, which consists of numerous randomly aggregated nanoparticles about 40 nm in size, is highly rough and porous. The effects of various reaction conditions on the morphology and size of the as-prepared samples were also investigated in detail. CaF_2 hollow spheres codoped with Ce^{3+} and Tb^{3+} show intense, bright green photoluminescence (PL) under UV irradiation with a quantum efficiency as high as 77%, based on efficient energy transfer from Ce^{3+} to Tb^{3+}. Desirable properties of these hierarchical particles as drug carriers were revealed by using ibuprofen as a model drug. Therefore, the as-obtained monodisperse, luminescent, and mesoporous hollow spheres have potential applications in lighting and drug delivery.

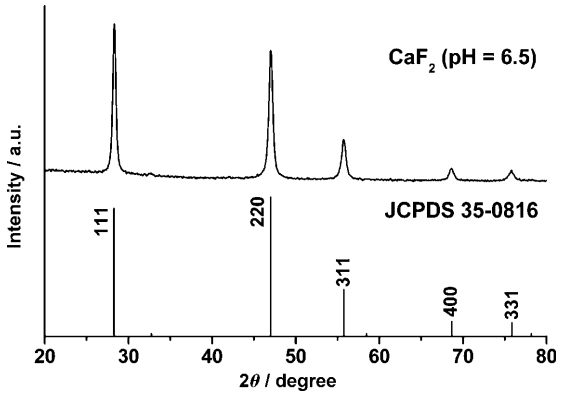

Figure 1. XRD pattern of the CaF_2 sample prepared at 180°C for 24 h (pH 6.5) and the standard data of CaF_2 (JCPDS No. 35-0816) as reference.

Results and Discussion

Phase structure, morphology, and formation process: Monodisperse CaF_2 hollow spheres were synthesized hydrothermally at pH 6.5 and 180°C for 24 h. Figure 1 shows the XRD pattern of as-prepared CaF_2 sample and the standard data for CaF_2 (JCPDS No. 35-0816). All of the diffraction peaks of the XRD pattern can be indexed as pure cubic phase, and coincide well with the standard data of CaF_2 (JCPDS No. 35-0816, space group $Fm\bar{3}m$, No. 225). The absence of any detectable peak shift or other phase in the XRD pattern indicates that the pure CaF_2 phase can be obtained under the above conditions by this simple method. The strong and sharp diffraction peaks of the sample indicate that the as-obtained CaF_2 sample is well crystallized.

Figure 2 shows SEM, TEM, and HRTEM images of the as-prepared CaF_2 sample. The low- and high-magnification SE micrographs in Figure 2a and b show that monodisperse and uniform hollow spheres can be prepared by this approach. The diameters of the hollow spheres are about 480 nm. The high-magnification SEM image (Figure 2b) of the CaF_2 sample provides detailed structural information on the spheres. The broken CaF_2 spheres confirm the hollow structure. Furthermore, the peripheral surface of individual hollow spheres is not smooth and contains many dense nanoparticles with diameters of around 40 nm. Figure 2c shows a typical TEM image of the CaF_2 hollow spheres,

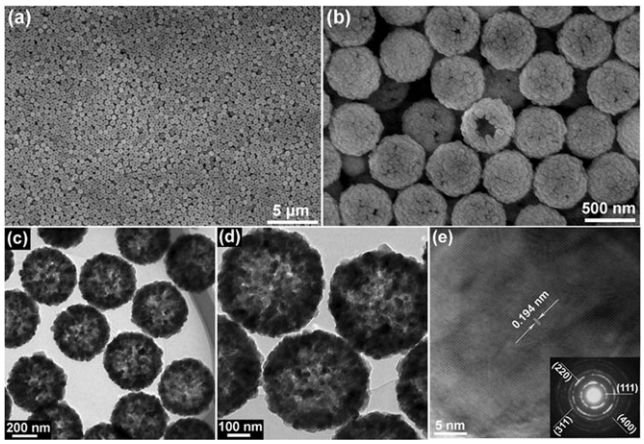

Figure 2. SEM (a, b), TEM (c, d), and HRTEM (e) images of as-prepared CaF_2 hollow spheres (180°C, pH 6.5, 24 h). Inset in part e is the SAED pattern.

which further confirms the uniform size and hollow structure of the CaF_2 spheres. The high-magnification TEM image in Figure 2d shows clearly the stacking of the building blocks and the interior cavity of the sphere, since the contrast at the center is much lower than that of a solid particle. In the selected-area electron diffraction (SAED) pattern (inset in Figure 2e), the strong concentric ring patterns can be indexed to the (111), (220), (311), and (400) planes of CaF_2 phase, respectively, and demonstrate its polycrystalline nature. As disclosed by the corresponding HRTEM image (Figure 2e), the interplanar distance between the adjacent lattice fringes is 0.194 nm. This plane can be indexed as the *d* spacing of the (220) plane of CaF_2 crystal.

To reveal the growth process of CaF_2 hollow spheres, time-dependent experiments were carried out (pH 6.5) by keeping other reaction parameters unchanged. Figure 3

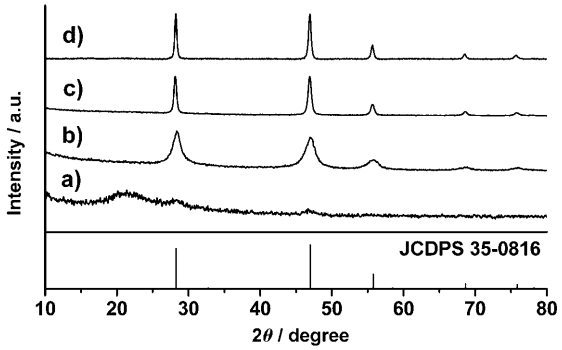

Figure 3. XRD patterns of the as-prepared samples at 180 °C for different reaction times. a) 0.5, b) 1, c) 6, and d) 48 h. These samples were prepared under the same conditions as the sample prepared at 180 °C for 24 h.

shows the XRD patterns of the products prepared at different reaction times. The XRD pattern of the sample obtained at 180 °C for 0.5 h shows a broad and weak band at 18–25° (Figure 3a), which indicates that the sample is amorphous. We assumed that this sample is a complex formed by Ca^{2+} cations and citrate (Cit^{3-}) anions, which is confirmed by the FTIR spectrum (see Figure S1 in the Supporting Information). At an early growth stage (0.5 h), the FTIR spectrum of the product is very similar to that of commercial trisodium citrate, that is, a Ca^{2+}–citrate complex formed in the early stages of the reaction. When the reaction time extends to 1 h or longer, all diffraction peaks of the as-obtained samples can be indexed to the cubic phase of CaF_2 (Figure 3b–d), that is, pure CaF_2 is formed. The diffraction peaks of the CaF_2 samples become sharper and stronger with increasing reaction, that is, the nanoparticles on the surface of the hollow spheres grow gradually, and the crystallinity increases with increasing reaction time.

The SEM images of the products obtained after different times at the same hydrothermal temperature (180 °C) are shown in Figure 4. After 0.5 h the amorphous intermediate consists of uniform spheres (ca. 480 nm) with smooth surface (Figure 4a). The TEM image (inset in Figure 4a) reveals a solid structure, and no hollow spheres are present. A coarse surface appears instead of the smooth surface on increasing the reaction time to 1 h (Figure 4b). This change indicates formation of the crystalline CaF_2. After 6 h of growth, the morphology changes slightly. The size of nanoparticles on the surface and the crystallinity increase (Figure 4c). When the reaction time is prolonged to 24 h, the nanoparticles on the surface can be observed even more clearly, and hollow spheres are obtained (Figure 2). When the reaction proceeds for a further 48 h, the spherical structure is preserved, but the surfaces of the spheres change. The nanoparticles on the surface of the spheres become even more evident and the size of the nanoparticles further increases to about 70 nm. Thus, the surface of the spheres becomes coarser and the nanoparticle size increases with increasing reaction time, which may be due to increased crystallinity. In addition, the hollow CaF_2 spheres are formed by transformation of the intermediate solid spheres.

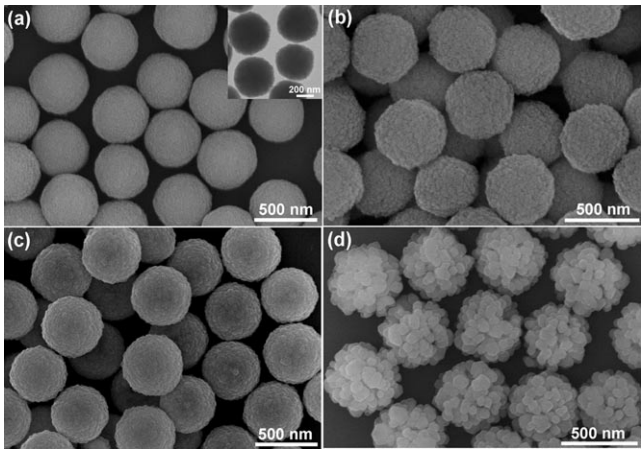

Figure 4. SEM images of the as-prepared CaF_2 samples at 180 °C for different reaction times. a) 0.5 (inset: TEM image), b) 1.0, c) 6, and d) 48 h.

According to the above analysis, the formation mechanism of the CaF_2 hollow spheres depends on a series of chemical and structural transformations. During the process, trisodium citrate plays a critical role in controlling the morphology of the final CaF_2 products. To investigate the effect of trisodium citrate on shape evolution, a control experiment was carried out in the absence of trisodium citrate, while other parameters remained identical. The as-synthesized CaF_2 sample was composed of irregular particles on a large scale with broad size distribution (see Figure S2 in the Supporting Information). The detailed formation process of the CaF_2 hollow spheres can be summarized as follows. In the early stage of the reaction, uniform Ca^{2+}–Cit^{3-} intermediate solid spheres are formed, as confirmed by FTIR, SEM, and TEM analysis (see Figure S1 in the Supporting Information and Figure 4a). The as-obtained intermediate was employed as both physical and chemical template, which not only cast the morphology of the product but also afforded a reactant source for an interfacial reaction. As F^- ions can be released from BF_4^- in aqueous solution, the

CaF_2 nuclei were formed by surface deposition and a subsequent crystal growth process, during which F^- deposited onto the surface of the intermediate solid spheres and reacted with the inner core to generate CaF_2 nuclei. As the reaction continued, the intermediate was consumed gradually and the formed CaF_2 nuclei grew into CaF_2 nanoparticles. The CaF_2 nanoparticles further aggregate to form CaF_2 shells.[35–37] With further reaction, CaF_2 hollow spheres are obtained by evacuation of the intermediate solid spheres, which is believed to be the result of the Ostwald ripening mechanism induced by a chemical transformation.[29,38–42] During the ripening process, the inner crystallites would dissolve and migrate outwards, leaving channels connecting the inner and outer spaces in the CaF_2 shells.[29] The solid cores could be excavated with enough ripening time due to the higher surface energy. Once the cores in the center of the microspheres are consumed completely, hollow microspheres are formed.[29,36,39] The probable reaction process for the formation of CaF_2 hollow spheres may be summarized as Equations (1)–(3).

$$Ca^{2+} + Cit^{3-} \rightarrow Ca^{2+} - Cit^{3-}\ (\text{complex}) \quad (1)$$

$$BF_4^- + 3\,H_2O \rightarrow 3\,HF + F^- + H_3BO_3 \quad (2)$$

$$Ca^{2+} - Cit^{3-} + 2\,F^- \rightarrow CaF_2 + Cit^{3-} \quad (3)$$

A schematic of the possible formation process of the CaF_2 hollow spheres is presented in Scheme 1.

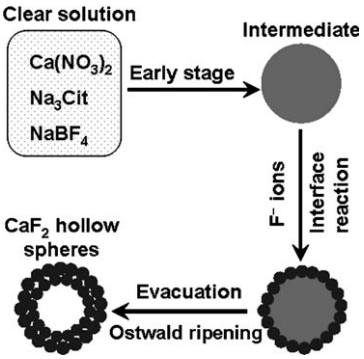

Scheme 1. Schematic illustration of the formation process of the CaF_2 hollow spheres.

The size of the hollow CaF_2 spheres is critically dependent on the pH value during the hydrothermal process. Hence, we performed control experiments at different pH values (180 °C, 24 h). All products prepared at different pH values (see Figure S3 in the Supporting Information) can be indexed as pure, well-crystallized, cubic CaF_2 (JCPDS No. 35-0816), in good accordance with the XRD pattern in Figure 1. However, the size and hollow structure change in comparison with the CaF_2 sample obtained at pH 6.5 (Figure 2a and b). Figures 5 and 6 show SEM and TEM images of the CaF_2 samples, respectively. When the pH value of the initial solution is adjusted to 7.0, the size of the hollow spheres decreases to about 300 nm, and the hollow structure is quite unstable and easily broken (Figure 5a and b). The nanoparticles constituting the shells tend to become loose in comparison with those of CaF_2 obtained at pH 6.5 (Figure 2a and b). Figure 6a shows a typical TEM image of CaF_2 hollow spheres with a size of about 300 nm (pH 7.0). It shows clearly the hollow structure, interior cavity, and building blocks of the hollow spheres (inset in Figure 6a). When the pH value of the initial solution decreases to 6.0, the size of the CaF_2 hollow spheres increases to about 750 nm (Figure 5c and d). The corresponding TEM image shows the hollow structure of the as-formed sample with large particle size (Figure 6b). The shells of CaF_2 hollow spheres are also composed of nanoparticles. On further decreasing the pH to 5.0, the particle size of the CaF_2 sample further increases to about 930 nm (Figure 5e and f). The high-magnification SEM image (Figure 5f) of the sample indicates that the surface of each sphere contains numerous nanoparticles and is much smoother than that of other samples. The hollow structure of the microspheres can not be clearly seen in the TEM image (Figure 6c). The reason might be that the shell is too thick and the nanoparticles composing the shells are aggregated tightly. However, when an aqueous suspension of the sample was treated by ultrasonication for 30 min, some CaF_2 spheres were destroyed and the hollow structure could be observed clearly (see Figure S4 in the Supporting Information). These results indicate that all of the CaF_2 samples of different sizes have hollow structure.

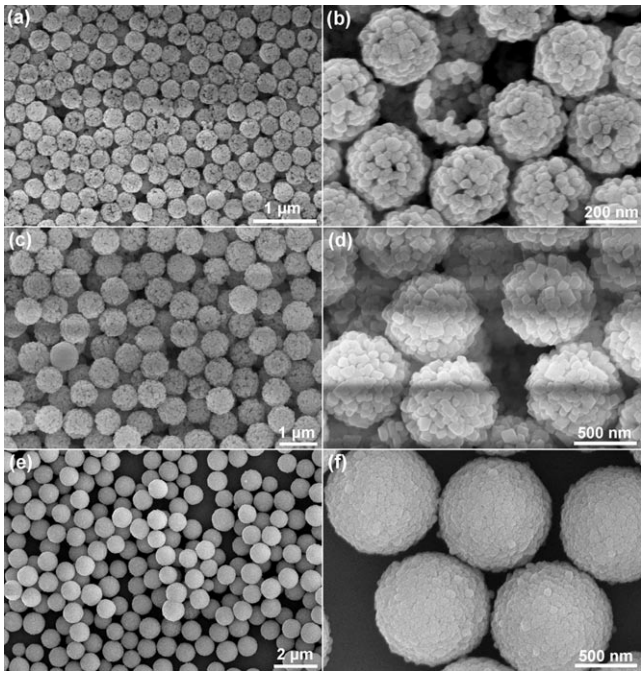

Figure 5. SEM images of CaF_2 samples obtained at different pH values in the original solution. a, b) 7.0; c, d) 6.0; and e, f) 5.0.

To investigate the specific surface area and porous nature of the CaF_2 hollow spheres, BET gas-sorption measurements

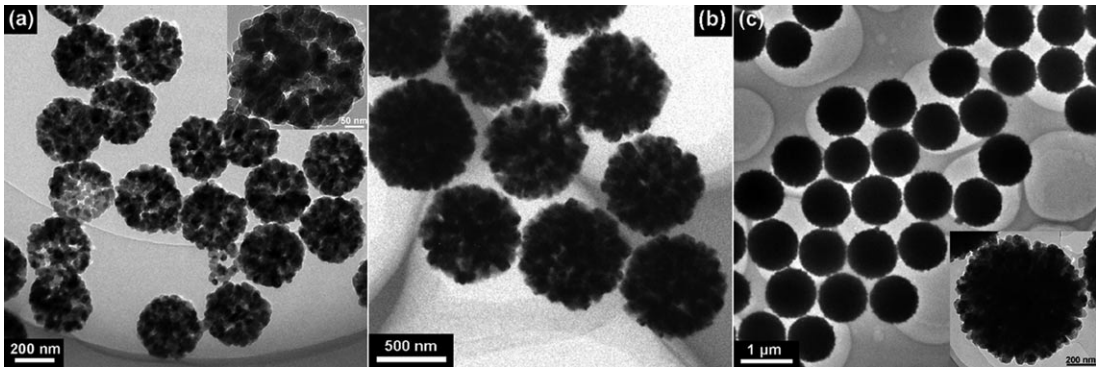

Figure 6. TEM images of CaF_2 samples synthesized at different pH values in the original solution. a) 7.0, b) 6.0, and c) 5.0.

were carried out. The CaF_2 hollow spheres with a size of 480 nm prepared at pH 6.5 were chosen as a representative sample to investigate the mesoporous properties owing to their stable and clearly hollow structure. Figure 7 shows the

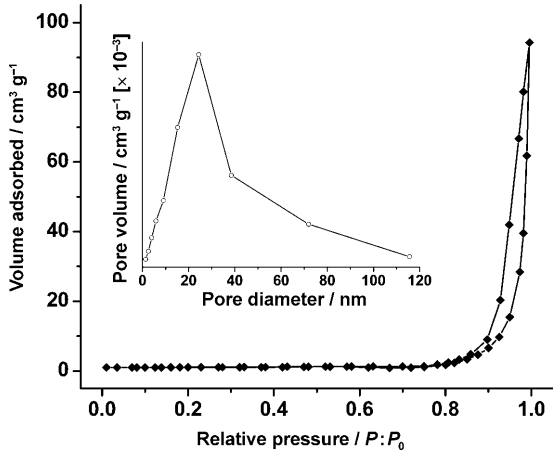

Figure 7. N_2 adsorption/desorption isotherms for CaF_2 hollow spheres prepared at pH 6.5. Inset: pore size distribution for the CaF_2 hollow spheres.

N_2 adsorption/desorption isotherm and pore size distribution of as-prepared CaF_2 sample. It can be seen that the CaF_2 hollow spheres show similar N_2 adsorption and desorption isotherms and typical H_1 hysteresis loops, which are properties of typical mesoporous materials. The BET surface area of the sample is about $17.7\,m^2g^{-1}$, the pore volume is $0.219\,cm^3g^{-1}$, and the pore-size distribution shows a narrow apex centered at 24.6 nm (inset in Figure 7). The pores are possibly attributable to the interstitial spaces between nanocrystals in the shell, which is in agreement with SEM and TEM observations (Figure 2). This result indicates that the as-prepared CaF_2 hollow spheres have porous structures.

The phase, morphology, and structure of the Ce^{3+}/Tb^{3+}-doped CaF_2 samples are identical with those of the pure CaF_2 sample, as confirmed by XRD, SEM, and TEM studies on CaF_2:Ce^{3+}/Tb^{3+} samples prepared at 180 °C and pH 6.5 for 24 h (see Figure S5 in the Supporting Information). Figure S5a of the Supporting Information shows that all diffraction peaks of the as-obtained CaF_2:Ce^{3+}/Tb^{3+} sample can be indexed to the cubic phase of CaF_2 (JCPDS No. 35-0816). The crystal cell parameters of CaF_2 and CaF_2:Ce^{3+}/Tb^{3+} samples were calculated from the XRD data. A slight decrease of the lattice constant for CaF_2:Ce^{3+}/Tb^{3+} ($a=0.5462$ nm) was observed with respect to that of pure CaF_2 hollow spheres ($a=0.5471$ nm). This is because eight-coordinate Ce^{3+} and Tb^{3+} have a smaller radius than the eight-coordinate Ca^{2+},[43] so the cubic lattice parameter of CaF_2 co-doped with Ce^{3+}/Tb^{3+} would shrink slightly in comparison with that of pure CaF_2.[44] No other peaks can be detected in the XRD pattern, and the slight change in lattice parameter confirms that the Ce^{3+} and Tb^{3+} ions have been effectively incorporated into the CaF_2 host lattice. The SEM and TEM images (see Figure S5b and c in the Supporting Information) show that the average size, morphology, and hollow structure of CaF_2:Ce^{3+}/Tb^{3+} (pH 6.5) are almost identical with those of the pure CaF_2 counterparts (Figure 2), that is, the dopant ions (Ce^{3+}/Tb^{3+}) have little effect on the morphology and crystallinity of CaF_2. In other words, Ce^{3+} and/or Tb^{3+} are well dissolved in CaF_2 crystals. To further confirm composition in the hollow spheres, CaF_2:Ce^{3+}/Tb^{3+} was subjected to XPS analysis. The narrow-scan XPS spectra of Ca 2p, F 1s, Ce 3d, and Tb 4d core level peaks are shown in Figure S6 in the Supporting Information. The XPS peaks can be readily assigned to the binding energy of Ca 2p, F 1s, Ce 3d, and Tb 4d, respectively.[45] The XPS results provide additional evidence for successful doping of Ce^{3+} and Tb^{3+} into CaF_2:Ce^{3+}/Tb^{3+}.

Photoluminescence properties of CaF_2:Ce^{3+}/Tb^{3+} hollow spheres: All of the CaF_2:Ce^{3+}/Tb^{3+} samples of different size exhibit a strong green emission under UV excitation. We selected the CaF_2:Ce^{3+}/Tb^{3+} hollow spheres with a size of 480 nm as a representative example to elucidate their luminescence properties. The CaF_2:Ce^{3+} sample shows UV emission centered at 338 nm on UV excitation (306 nm). The excitation and emission spectra of CaF_2:Ce^{3+} are shown in Figure 8. The excitation spectrum (Figure 8a) consists of a broad and strong band with a maximum at 306 nm and a weaker band at 258 nm, which corresponds to the transitions

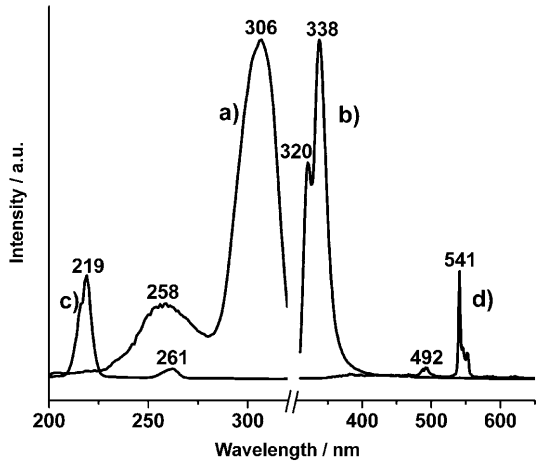

Figure 8. PL excitation and emission spectra for CaF_2:Ce^{3+} [a), λ_{em}= 338 nm; b) λ_{ex}=306 nm] and CaF_2:Tb^{3+} [c) λ_{em}=541 nm; d) λ_{ex}= 219 nm].

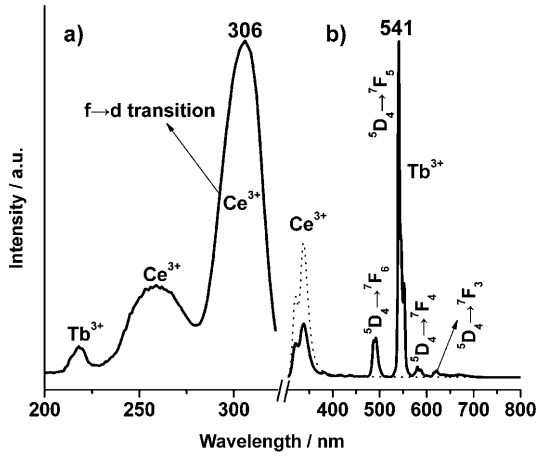

Figure 9. PL excitation (a) and emission (b) spectra for the as-synthesized CaF_2:Ce^{3+}/Tb^{3+}. The emission spectrum of CaF_2:Ce^{3+} is presented for comparison (dotted line).

from the $^2F_{5/2}$ ground state of Ce^{3+} to the different components of the excited Ce^{3+} 5d states split by the crystal field.[45,46] The emission spectrum of Ce^{3+} (Figure 8b) consists of two peaks at 320 and 338 nm respectively, which corresponds to the transitions from the lowest excited 5d state to the 4f ground state, and the doublet is a result of the ground-state splitting, that is, the $^2F_{5/2}$ and $^2F_{7/2}$ levels of Ce^{3+}.[46] This splitting, which is calculated to be about 1700 cm^{-1}, approaches the theoretical value of 2000 cm^{-1}.[47] The excitation and emission spectra of CaF_2:Tb^{3+} sample are also shown in Figure 8. The excitation spectrum (Figure 8c) consists of a strong band at 219 nm and a weak band at 261 nm, which correspond to the spin-allowed ($\Delta S=0$) and spin-forbidden ($\Delta S=1$) components of the $4f^8$–$4f^7$5d transition, respectively.[47] The calculated energy difference between these two bands of about 7300 cm^{-1} agrees well with the value in the literature.[48] On excitation into the $4f^8$–$4f^7$5d transition (219 nm), the CaF_2:Tb^{3+} hollow spheres yield the characteristic emission spectrum of Tb^{3+} (Figure 8d). The emission spectrum exhibits four lines centered at 491, 541, 580, and 620 nm, originating from transitions from the $^5D_4$ excited state to the ^7F_J ($J=6$, 5, 4, 3) ground states of Tb^{3+}, with the $^5D_4\rightarrow{}^7F_5$ transition at 541 nm as the most prominent group.

Figure 9a and b show the excitation and emission spectra of the Ce^{3+}/Tb^{3+}-codoped CaF_2 sample, and the inset shows a luminescence photograph of CaF_2:Ce^{3+}/Tb^{3+} hollow spheres under a 254 nm UV lamp in the dark, which exhibit strong and bright green emission. The excitation spectrum (Figure 9a) monitored at the 541 nm ($^5D_4\rightarrow{}^7F_5$ transition of Tb^{3+}) contains a weak band at 219 nm, a moderate band at 258 nm, and a strong broad band with a maximum at 306 nm. In comparison with the excitation spectra of CaF_2:Ce^{3+} and CaF_2:Tb^{3+} samples (Figure 8), we can ascribe the band at 219 nm to the $4f^8$–$4f^7$5d transitions of Tb^{3+} ions, and the bands at 258 and 306 nm to 5d–4f transitions of Ce^{3+} ions. The presence of the excitation bands of Ce^{3+} in the excitation spectrum monitored with Tb^{3+} emission indicates that energy transfer occurs from Ce^{3+} to Tb^{3+} in CaF_2:Ce^{3+}/Tb^{3+}. Excitation into the Ce^{3+} band at 306 nm yields both the weak emission of Ce^{3+} (310–370 nm, which is identical to the emission spectrum of CaF_2:Ce^{3+}) and the strong emission of Tb^{3+} ($^5D_4\rightarrow{}^7F_J$ at 491, 541, 580, and 620 nm; $J=6$, 5, 4, 3), as shown in Figure 9b, and is a further indication of energy transfer from Ce^{3+} to Tb^{3+} in CaF_2:Ce^{3+}/Tb^{3+} hollow spheres. The energy transfer efficiency from Ce^{3+} to Tb^{3+} can be calculated according to the formula $\eta_{ET}=1-I_d/I_{d0}$, where I_d and I_{d0} are the corresponding integrated luminescence intensities of the donor (Ce^{3+}) in the presence and absence of the acceptor (Tb^{3+}) for the same donor (Ce^{3+}) concentration, respectively. The energy-transfer efficiency from Ce^{3+} to Tb^{3+} in the current CaF_2:Ce^{3+}/Tb^{3+} system (with 2 mol% Ce^{3+} and 2 mol% Tb^{3+}) is 57%.[49] Since the critical distance R_c is as an important parameter in energy transfer, we calculated the R_c value of CaF_2:Ce^{3+}/Tb^{3+}. Considering the electric-dipole interaction, $R_c^6=0.6\times10^{28}\times4.8\times10^{-16}\times f_A\times E^{-4}\times SO$, where the oscillator strength $f_A(Tb^{3+})=10^{-6}$ (spin-forbidden narrow-line transitions of Tb^{3+}), $E=3.5413$ eV (the energy of maximum spectral overlap), and $SO=0.7576$ eV^{-1} (the normalized spectral overlap between the excitation lines of Tb^{3+} and the emission of Ce^{3+}), we obtain $R_c=0.49$ nm for CaF_2:Ce^{3+}/Tb^{3+} hollow spheres.[45,50] Although this critical distance is not very accurate, it indicates that energy transfer occurs mainly between nearest-neighbor Ce^{3+} and Tb^{3+}. The lifetime τ of luminescence for Tb^{3+} (detected at 541 nm for the $^5D_4\rightarrow{}^7F_5$ transition) is determined to be 9.6 ms. This is a typical lifetime for luminescence due to Tb^{3+} ions.[26] The PL quantum efficiency for the as-obtained CaF_2:Ce^{3+}/Tb^{3+} hollow spheres with a size of 480 nm is 70% under excitation at 306 nm. In addition, all of the CaF_2:Ce^{3+}/Tb^{3+} spheres of different sizes have similar shape and profile for the emission spectra except for the relative intensity (not shown).

Figure 10 shows the relationship between the integrated PL emission intensity and quantum efficiency of $CaF_2:Ce^{3+}/Tb^{3+}$ phosphors and the particle size. The emission intensity increases with increasing the size of the $CaF_2:Ce^{3+}/Tb^{3+}$

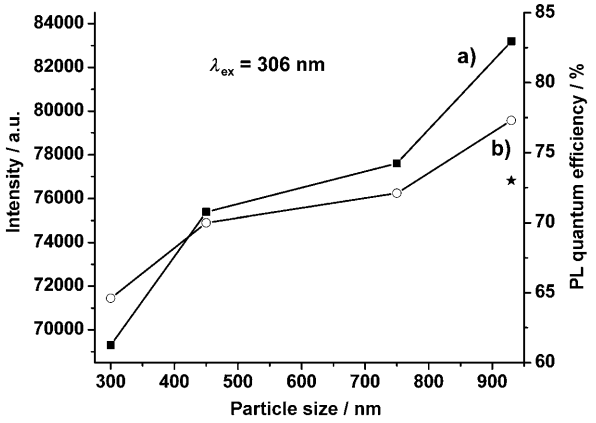

Figure 10. Integrated PL emission intensity (a) and PL quantum efficiency (b) of $CaF_2:Ce^{3+}/Tb^{3+}$ hollow spheres as a function of particle size. The quantum efficiency of commercial Ce^{3+}/Tb^{3+}-doped aluminate phosphor (star) is shown for comparison.

spheres. Larger particle size is well known to improve the PL intensity of phosphors.[51] In this case, the reason might be that the shell becomes thicker and the nanoparticles composing the shells congregate more tightly with increasing particle size. Moreover, the increasing amount of emitting Tb^{3+} ions on the surface with growing the size of the hollow spheres will result in enhanced PL intensity.[52] Furthermore, the enlargement of the crystallite size means a major decrease in bulk defects, which is also very beneficial for the luminescence efficiency of phosphor particles.[53] Accordingly, the PL quantum efficiency of the CaF_2 hollow spheres increases with increasing particle size (65% for 300 nm, 70% for 480 nm, 72% to 750 nm, and 77% for 930 nm), as shown in Figure 10b. In addition, the PL quantum efficiencies of the as-prepared $CaF_2:Ce^{3+}/Tb^{3+}$ samples can almost reach or even exceed that of commercial Ce^{3+}/Tb^{3+}-doped aluminate phosphor (star in Figure 10) under the same excitation conditions ($\lambda_{ex}=306$ nm). In Figure S7 of the Supporting Information, the chromaticity coordinates (CIE) of as-prepared $CaF_2:Ce^{3+}/Tb^{3+}$ and commercial Ce^{3+}/Tb^{3+}-doped aluminate phosphors are shown as points 1 ($x=0.2540$, $y=0.6667$) and 2 ($x=0.2583$, $y=0.6315$), respectively, located in the green region. Due to the strong photoluminescence intensity, uniform morphology, and excellent CIE chromaticity of as-prepared $CaF_2:Ce^{3+}/Tb^{3+}$ samples, they are potentially useful as efficient green-emitting components in photoluminescence applications such as fluorescent lamps, UV LEDs, and backlights.

Drug adsorption and release properties: Ibuprofen (IBU) was selected as a model drug to study the drug storage and release properties of this system. The FTIR spectra for $CaF_2:Ce^{3+}/Tb^{3+}$, IBU–$CaF_2:Ce^{3+}/Tb^{3+}$, and IBU are shown in Figure 11. In the FTIR spectrum of $CaF_2:Ce^{3+}/Tb^{3+}$ (Figure 11a), the broad band at 3431 cm^{-1} is ascribable to the O–H vibration of H_2O absorbed in the sample. The peaks appearing between 1400–1600 cm^{-1} arise from the ν(C=O) stretching mode,[54] which might be due to addition of Cit^{3-} ions in the hydrothermal process. For IBU-loaded $CaF_2:Ce^{3+}/Tb^{3+}$ (Figure 11b), the band assigned to the COOH vibration at 1714 cm^{-1} can be compared with that of commercial IBU (Figure 11c). Furthermore, the absorption band assigned to the quaternary carbon atom located at 1467 cm^{-1}, $C-H_x$ bonds at 2868 and 2958 cm^{-1}, and other weak peaks at 750–1300 cm^{-1} can also be observed,[55] and confirm the successful adsorption of IBU onto the surface of the mesoporous $CaF_2:Ce^{3+}/Tb^{3+}$ hollow spheres. A degree of IBU loading for $CaF_2:Ce^{3+}/Tb^{3+}$ hollow spheres of 7.2 wt% was determined by thermogravimetric (TG) analysis. The TG curves of the as-prepared $CaF_2:Ce^{3+}/Tb^{3+}$ sample and IBU–$CaF_2:Ce^{3+}/Tb^{3+}$ sample are shown in Figure S8 of the Supporting Information. The greatest loss of ibuprofen occurs at 200–550 °C for the IBU-loaded $CaF_2:Ce^{3+}/Tb^{3+}$ sample. This result is similar to a previous report,[56] which further confirms loading of ibuprofen into the $CaF_2:Ce^{3+}/Tb^{3+}$ sample. The cumulative drug release profiles for the IBU–$CaF_2:Ce^{3+}/Tb^{3+}$ systems as a function of release time in simulated body fluid are shown in Figure 12A. The system shows a burst release of about 60% within 0.5 h and nearly 88% within 1 h followed by relatively slow release and complete release after 2 h. The initial burst release may be attributed to IBU weakly adsorbed on the outer surface of the mesoporous $CaF_2:Ce^{3+}/Tb^{3+}$ hollow spheres, and the slow release of the remaining of IBU may be due to adsorption on the internal surface of the hollow spheres.

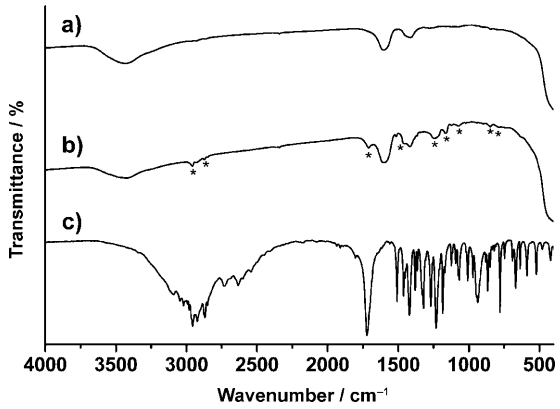

Figure 11. FTIR spectra of $CaF_2:Ce^{3+}/Tb^{3+}$ (a), IBU–$CaF_2:Ce^{3+}/Tb^{3+}$ (b), and commercial IBU (c).

In addition, the PL emission intensity of IBU–$CaF_2:Ce^{3+}/Tb^{3+}$ sample is affected by the cumulative amount of released IBU. Figure 12B shows the PL emission spectra of IBU–$CaF_2:Ce^{3+}/Tb^{3+}$ at different release times. The PL intensity increases with increasing release time. Since the cumulative amount of IBU released from IBU–$CaF_2:Ce^{3+}/Tb^{3+}$ is in direct proportion to the release time, it can be concluded that the PL intensity increases with increasing cu-

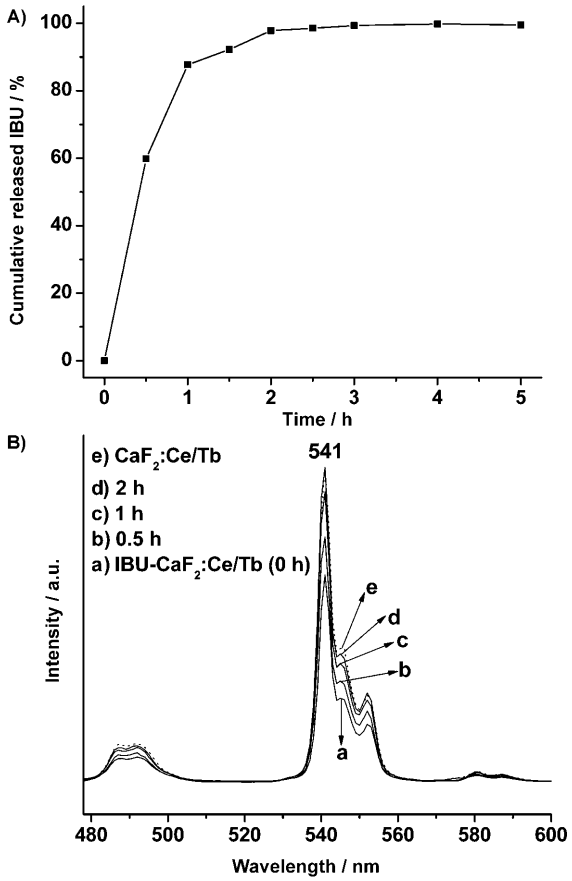

Figure 12. A) Cumulative IBU release from IBU–CaF_2:Ce^{3+}/Tb^{3+} as a function of release time in SBF. B) PL emission spectra of IBU–CaF_2:Ce^{3+}/Tb^{3+} at different release times. a) 0, b) 0.5, c) 1, and d) 2 h. e) Emission spectrum of CaF_2:Ce^{3+}/Tb^{3+} without IBU loading (dotted line).

mulative amount of released IBU and reaches a maximum when IBU is completely released. The reason might be that IBU molecules can be adsorbed onto the surface of mesoporous CaF_2:Ce^{3+}/Tb^{3+} hollow spheres, and the organic groups in IBU with high vibrational frequencies from 1000 to 3500 cm^{-1} will strongly quench the emission of Tb^{3+} in IBU–CaF_2:Ce^{3+}/Tb^{3+}.[53] The quenching effect would disappear and the PL intensity be almost restored when the release of IBU from CaF_2:Ce^{3+}/Tb^{3+} sample is complete, as shown in Figure 12 B. This characteristic may have potential as a probe for monitoring or tracking the drug release process, that is, the CaF_2:Ce^{3+}/Tb^{3+} hollow spheres can be potentially used as a smart drug carrier.

Conclusion

Through a simple synthetic route, mesoporous CaF_2 and luminescence-functionalized CaF_2:Ce^{3+}/Tb^{3+} hollow spheres were obtained. The as-prepared CaF_2:Ce^{3+}/Tb^{3+} samples show uniform hollow spherical morphology and mesoporous structure which is suitable for use as a drug carrier. For CaF_2:Ce^{3+}/Tb^{3+} samples, a strong green emission with high PL quantum efficiency centered at about 541 nm can be observed at room temperature under UV excitation. Drug storage/release properties of the luminescent CaF_2:Ce^{3+}/Tb^{3+} hollow spheres were demonstrated for ibuprofen. The as-obtained monodisperse CaF_2:Ce^{3+}/Tb^{3+} hollow spheres can thus be used to encapsulate chemicals and release them, and hence these materials may find potential applications in the fields of luminescence, drug delivery, and disease therapy, based on their well-dispersed and uniform luminescent and mesoporous properties.

Experimental Section

Chemicals and materials: Tb_4O_7 and $Ce(NO_3)_3{\cdot}6H_2O$ with purity of 99.99% were purchased from Changchun Applied Chemistry Science and Technology Limited, China. Tb_4O_7 was dissolved in dilute HNO_3, and residual HNO_3 was removed by heating and evaporation to give clear solutions of $Tb(NO_3)_3$. $Ce(NO_3)_3{\cdot}6H_2O$ was dissolved in water to form a clear solution. Ibuprofen (IBU) was purchased from Nanjing Chemical Regent Co., Ltd. Other chemicals were analytical-grade reagents purchased from Beijing Chemical Corporation. All starting materials were used without further purification.

Preparation of CaF_2 and CaF_2:Ce^{3+}/Tb^{3+} hollow spheres: The mesoporous CaF_2 hollow spheres were prepared by a hydrothermal process. In a typical experiment, 2 mmol of $Ca(NO_3)_2{\cdot}4H_2O$ and 4 mmol of trisodium citrate (Cit^{3-}) were dissolved in deionized water to form 40 mL of solution 1. Then, 4 mmol of $NaBF_4$ was added to 20 mL H_2O to form solution 2. After vigorously stirring for 15 min, solution 2 was added to solution 1, and ammonia (or HNO_3) solution was added to adjust the pH value. After additional agitation for 20 min, the as-obtained clear solution was transferred into a Teflon bottle (80 mL) held in a stainless steel autoclave, sealed, and maintained at 180 °C for 24 h. After allowing the autoclave to cool to room temperature, the obtained precipitate was separated by centrifugation and washed with deionized water and then ethanol. Finally, the precipitate was separated by centrifugation again and dried in air at 70 °C for 24 h to obtain the final CaF_2 hollow spheres. Hydrothermal treatment in the absence of trisodium citrate and for different reaction times was performed to investigate the morphological evolution of the CaF_2 hollow spheres.

The luminescent CaF_2: Ce^{3+}/Tb^{3+} hollow spheres were prepared by the same procedure as above, except that aqueous solutions of $Tb(NO_3)_3$ (2 mol% vs. Ca^{2+}) and/or $Ce(NO_3)_3$ (2 mol% vs. Ca^{2+}) were initially added to solution 1.

Preparation of drug storage/delivery systems: The drug storage system using luminescence functionalized mesoporous CaF_2: Ce^{3+}/Tb^{3+} hollow spheres with a size of 480 nm as a carrier was prepared according to previous reports.[57,58] Ibuprofen was selected as the model drug. Typically, 0.1 g of luminescent CaF_2: Ce^{3+}/Tb^{3+} was added to 20 mL of a 60 mg mL^{-1} solution of IBU in hexane at room temperature, and allowed to soak for 24 h with stirring in a vial, which was sealed to prevent the evaporation of hexane. The IBU-loaded CaF_2:Ce^{3+}/Tb^{3+}sample, denoted as IBU–CaF_2: Ce^{3+}/Tb^{3+}, was separated by centrifugation, and then dried at 70 °C for 24 h.

Release of IBU was investigated in simulated body fluid (SBF) with slow stirring at 37 °C. The ionic composition of the as-prepared SBF solution was similar to that of human body plasma with a molar composition of 142.0/5.0/2.5/1.5/147.8/4.2/1.0/0.5 for Na^+/K^+/Ca^{2+}/Mg^{2+}/Cl^-/HCO_3^-/HPO_4^{2-}/SO_4^{2-} (pH 7.4).[58] The amount of IBU adsorbed onto the mesoporous CaF_2: Ce^{3+}/Tb^{3+} sample was determined by thermogravimetric (TG) analysis. The amount of IBU released from the IBU–CaF_2:Ce^{3+}/Tb^{3+} sample was monitored by UV/Vis spectroscopy at 220 nm.

Characterization: The X-ray diffraction (XRD) patterns of the samples were recorded on a D8 Focus diffractometer (Bruker) with $Cu_{K\alpha}$ radiation ($\lambda = 0.15405$ nm). FTIR spectra were recorded on a Perkin-Elmer

580B IR spectrophotometer in KBr pellets. The morphology of the samples was inspected with a scanning electron microscope (SEM; S-4800, Hitachi). Transmission electron microscopy (TEM) and high-resolution transmission electron microscopy (HRTEM) images were obtained with an FEI Tecnai G2 S-Twin transmission electron microscope with a field-emission gun operating at 200 kV. Nitrogen adsorption/desorption analysis was performed with a Micromeritics ASAP 2020M apparatus. The specific surface area was determined by the Brunauer–Emmett–Teller (BET) method. Thermogravimetric (TG) analysis (Perkin-Elmer Pyris Diamond) was used to determine the amount of IBU loaded onto the materials. The X-ray photoelectron spectra (XPS) were recorded on a VG ESCALAB MK II electron-energy spectrometer with $Mg_{K\alpha}$ (1253.6 eV) as the X-ray excitation source. The photoluminescence (PL) measurements were performed on a Hitachi F-4500 spectrophotometer equipped with a 150 W xenon lamp as excitation source. The luminescence decay curves were obtained from a Lecroy Wave Runner 6100 digital oscilloscope (1 GHz) by using a tunable laser (pulse width = 4 ns, gate = 50 ns) as excitation source (Continuum Sunlite OPO). The quantum efficiency of the phosphor samples was determined on a quantum-yield measurement system (C9920-02, Hamamatsu Photonics K.K., Japan). The UV/Vis adsorption spectral data were measured on a TU-1901 spectrophotometer. All measurements were performed at room temperature.

Acknowledgements

This project is financially supported by National Basic Research Program of China (2007CB935502, 2010CB327704), and the National Natural Science Foundation of China (NSFC 50872131, 60977013, 20901074, 20921002).

[1] F. Caruso, R. A. Caruso, H. Mohwald, *Science* **1998**, *282*, 1111–1114.
[2] F. Caruso, *Adv. Mater.* **2001**, *13*, 11–22.
[3] W. Wei, G. H. Ma, G. Hu, D. Yu, T. Mcleish, Z. G. Du, Z. Y. Shen, *J. Am. Chem. Soc.* **2008**, *130*, 15808–15810.
[4] S. W. Kim, M. Kim, W. Y. Lee, T. Hyeon, *J. Am. Chem. Soc.* **2002**, *124*, 7642–7643.
[5] X. W. Low, L. A. Archer, Z. C. Yang, *Adv. Mater.* **2008**, *20*, 3987–4019.
[6] Y. D. Yin, R. M. Rioux, C. K. Erdonmez, S. Hughes, G. A. Somorjai, P. Alivisatos, *Science* **2004**, *304*, 711–714.
[7] U. Jeong, Y. L. Wang, M. Ibisate, Y. N. Xia, *Adv. Funct. Mater.* **2005**, *15*, 1907–1921.
[8] P. Jiang, J. F. Bertone, V. L. Colvin, *Science* **2001**, *291*, 453–457.
[9] K. P. Velikov, A. V. Blaaderen, *Langmuir* **2001**, *17*, 4779–4786.
[10] Y. Wang, F. B. Su, J. Y. Lee, X. S. Zhao, *Chem. Mater.* **2006**, *18*, 1347–1353.
[11] F. Caruso, X. Shi, R. A. Caruso, A. Susha, *Adv. Mater.* **2001**, *13*, 740–744.
[12] Y. Lu, J. McLellan, Y. N. Xia, *Langmuir* **2004**, *20*, 3464–3470.
[13] X. M. Sun, Y. D. Li, *Angew. Chem.* **2004**, *116*, 3915–3919; *Angew. Chem. Int. Ed.* **2004**, *43*, 3827–3831.
[14] G. Jia, M. Yang, Y. H. Song, H. P. You, H. J. Zhang, *Cryst. Growth Des.* **2009**, *9*, 301–307.
[15] J. Gao, B. Zhang, X. Zhang, B. Xu, *Angew. Chem.* **2006**, *118*, 1242–1245; *Angew. Chem. Int. Ed.* **2006**, *45*, 1220–1223.
[16] Y. Sun, B. Mayers, Y. N. Xia, *Adv. Mater.* **2003**, *15*, 641–646.
[17] H. G. Yang, H. C. Zeng, *Angew. Chem.* **2004**, *116*, 5318–5321; *Angew. Chem. Int. Ed.* **2004**, *43*, 5206–5209.
[18] Y. Li, J. Shi, Z. Hua, H. Che, M. Ruan, D. Yan, *Nano Lett.* **2003**, *3*, 609–612.
[19] L. Qi, J. Li, J. Ma, *Adv. Mater.* **2002**, *14*, 300–303.
[20] X. Gao, J. Zhang, L. Zhang, *Adv. Mater.* **2002**, *14*, 290–293.
[21] J. X. Huang, Y. Xie, B. Li, Y. Liu, Y. T. Qian, S. Y. Zhang, *Adv. Mater.* **2002**, *14*, 808–811.
[22] Y. R. Ma, L. M. Qi, J. M. Ma, H. M. Cheng, *Langmuir* **2003**, *19*, 4040–4042.
[23] W. Z. Zheng, C. P. Chen, Q. P. Zhong, *Adv. Funct. Mater.* **2007**, *17*, 425–430.
[24] H. Yu, J. Yu, S. Liu, S. Mann, *Chem. Mater.* **2007**, *19*, 4327–4334.
[25] C. Feldmann, M. Roming, K. Trampert, *Small* **2006**, *2*, 1248–1250.
[26] Z. W. Quan, D. M. Yang, P. P. Yang, X. M. Zhang, H. Z. Lian, X. M. Liu, J. Lin, *Inorg. Chem.* **2008**, *47*, 9509–9517.
[27] P. Gao, Y. Xie, Z. Li, *Eur. J. Inorg. Chem.* **2006**, 3261–3265.
[28] Y. B. Mao, F. Zhang, S. S. Wong, *Adv. Mater.* **2006**, *18*, 1895–1899.
[29] W. S. Wang, L. Zhen, C. Y. Xu, J. Z. Chen, W. Z. Shao, *ACS Appl. Mater. Interfaces* **2009**, *1*, 780–788.
[30] R. Singh, S. Sinha, P. Chou, N. J. Hsu, F. Radpour, *J. Appl. Phys.* **1989**, *66*, 6179–6181.
[31] N. S. Sokolov, S. M. Suturin, *Thin Solid Films* **2000**, *367*, 112–119.
[32] T. Pilvi, K. Arstila, M. Leskelä, M. Ritala, *Chem. Mater.* **2007**, *19*, 3387–3392.
[33] X. M. Sun, Y. D. Li, *Chem. Commun.* **2003**, 1768–1769.
[34] T. Balaji, G. Lifante, E. Daran, R. Legros, G. Lacoste, *Thin Solid Films* **1999**, *339*, 187–193.
[35] G. Chen, S. Sun, W. Zhao, S. Xu, T. You, *J. Phys. Chem. C* **2008**, *112*, 20217–20221.
[36] J. J. Miao, L. P. Jiang, C. Liu, J. M. Zhu, J. J. Zhu, *Inorg. Chem.* **2007**, *46*, 5673–5677.
[37] H. Zhu, J. Wang, D. Wu, *Inorg. Chem.* **2009**, *48*, 7099–7104.
[38] J. Li, H. C. Zeng, *J. Am. Chem. Soc.* **2007**, *129*, 15839–15847.
[39] J. G. Yu, H. T. Guo, S. A. Davis, S. Mann, *Adv. Funct. Mater.* **2006**, *16*, 2035–2041.
[40] J. G. Yu, H. G. Yu, H. T. Guo, M. Li, S. Mann, *Small* **2008**, *4*, 87–91.
[41] B. Liu, H. C. Zeng, *Small* **2005**, *1*, 566–571.
[42] W. S. Wang, L. Zhen, C. Y. Xu, W. Z. Shao, *J. Phys. Chem. C* **2008**, *112*, 14360–14366.
[43] R. D. Shannon, *Acta Crystallogr. Sect. A* **1976**, *32*, 751–767.
[44] G. Jia, Y. Huang, Y. Song, M. Yang, L. Zhang, H. You, *Eur. J. Inorg. Chem.* **2009**, 3721–3726.
[45] Z. L. Wang, Z. W. Quan, P. Y. Jia, C. K. Lin, Y. Luo, Y. Chen, J. Fang, W. Zhou, C. J. O'Connor, J. Lin, *Chem. Mater.* **2006**, *18*, 2030–2037.
[46] A. Gektin, N. Shiran, V. Nesterkina, Y. Boyarintseva, V. Baumer, G. Stryganyuk, K. Shimamura, E. Villora, *J. Lumin.* **2009**, *129*, 1538–1541.
[47] J. Lin, Q. Su, *J. Mater. Chem.* **1995**, *5*, 1151–1154.
[48] G. Blasse, A. Bril, *Philips Res. Rep.* **1967**, *22*, 481–504.
[49] M. Yu, J. Lin, J. Fu, Y. C. Han, *Chem. Phys. Lett.* **2003**, *371*, 178–183.
[50] G. Blass, *Philips Res. Rep.* **1969**, *24*, 131–144.
[51] M. Yu, H. Wang, C. K. Lin, G. Z. Li, J. Lin, *Nanotechnology* **2006**, *17*, 3245–3252.
[52] C. K. Lin, D. Y. Kong, X. M. Liu, H. Wang, M. Yu, J. Lin, *Inorg. Chem.* **2007**, *46*, 2674–2681.
[53] K. Y. Jungz, K. H. Han, *Electrochem. Solid-State Lett.* **2005**, *8*, H17–H20.
[54] X. M. Zhang, Z. W. Quan, J. Yang, P. P. Yang, H. Z. Lian, J. Lin, *Nanotechnology* **2008**, *19*, 075603.
[55] P. P. Yang, Z. W. Quan, C. X. Li, X. J. Kang, H. Z. Lian, J. Lin, *Biomaterials* **2008**, *29*, 4341–4347.
[56] F. Xu, L. X. Sun, Z. C. Tan, J. G. Liang, R. L. Li, *Thermochim. Acta* **2004**, *412*, 33–37.
[57] I. I. Slowing, B. G. Trewyn, S. Giri, V. S. Y. Lin, *Adv. Funct. Mater.* **2007**, *17*, 1225–1236.
[58] M. Vallet-Regi, A. Rámila, R. P. Del Real, J. Pérez-Pariente, *Chem. Mater.* **2001**, *13*, 308–311.

Received: November 16, 2009
Published online: April 13, 2010

